Anion photoelectron spectroscopy of B_3N^-

Knut R. Asmis, Travis R. Taylor, and Daniel M. Neumark
Department of Chemistry, University of California, Berkeley, California 94720
and Chemical Sciences Division, Lawrence Berkeley National Laboratory, Berkeley, California 94720

(Received 9 August 1999; accepted 14 September 1999)

Vibrationally resolved negative ion photoelectron spectra of B_3N^- at 355 and 266 nm are presented. Two intense bands are observed with adiabatic detachment energies (ADEs) of 2.923 ± 0.008 eV and 3.063 ± 0.008 eV and markedly different photoelectron angular distributions. Aided by electronic structure calculations, the two bands are assigned to transitions from the linear $\tilde{X}\,^4\Sigma^-$ state of B_3N^- to the linear $^3\Pi$ and $^5\Sigma^-$ electronically excited states of neutral B_3N, with all three states having a B–N–B–B structure. Weak signal observed at lower electron binding energies is tentatively assigned to two additional linear-to-linear transitions from the low-lying electronically excited $^2\Pi$ state of B_3N^- to the $^1\Sigma^+$ and $^3\Pi$ states of neutral B_3N. Based on these assignments the electron affinity of linear B–N–B–B is 2.098 ± 0.035 eV. It remains uncertain if the $^1\Sigma^+$ state of linear B–N–B–B or the $^3A_1$ state of cyclic B_3N is the overall ground state. At the highest level of theory used here, CCSD(T)/aug-cc-pVTZ, the $^1\Sigma^+$ state is predicted to lie 0.09 eV below the $^3A_1$ state.
 [S0021-9606(99)00746-1]

I. INTRODUCTION

Boron nitride clusters play an important role as precursors in the formation of ultra-hard boron nitride films, which have received considerable attention in material science, due to the favorable properties these films exhibit for industrial applications.[1] However, spectroscopic studies on boron nitride clusters remain scarce. An intriguing aspect related to research on boron nitride clusters is the question of the cluster geometry and its dependence on cluster size, particularly in light of the extensive work on carbon clusters showing the evolution from linear to cyclic to fullerene structures with increasing size.[2–7] Clusters of the type $(BN)_n$ are isoelectronic with C_{2n}, so it is of interest to see if similar trends occur in boron nitride clusters in which both size and stoichiometry (B/N ratio) can be varied. In the larger size regime boron nitride nanostructures, both tube-like[8–10] and spherical,[11–13] can be produced. For small boron nitride clusters, including B_2N, B_2N^-, B_2N^+, BN_2, B_2N_2, and BN_3, only linear structures have been experimentally observed.[14–20]

Since C_4 is the smallest carbon cluster for which a cyclic structure is predicted to be either the ground state or a low-lying excited state,[21] tetra-atomic boron nitride clusters are of particular interest. In this article we present photoelectron spectra of B_3N^- in order to probe the spectroscopy and structure of B_3N and B_3N^-. Neither of these species has received much attention in the literature. Becker and co-workers[22,23] have observed singly-charged ions of B_3N in the mass spectrum from laser ablation of boron nitride, where clusters of the type $B_{x+1}N_x$ are found to dominate.[24] No experimental spectroscopic data exist on charged or neutral B_3N species.

Slanina, Martin, and co-workers[25–27] performed the only previous theoretical studies on the electronic structure of neutral B_3N. They found various stable isomers of B_3N of which the linear B–N–B–B arrangement presented the global minimum. A triangular $^1A_1'$ state, with the N atom occupying the central position, was found 0.53 eV higher in energy than the linear $^1\Sigma^+$ ground state. Planar structures with a B_3 ring and an N atom attached to the outside and linear N–B–B–B species were calculated to lie considerably higher in energy. Harmonic frequencies were determined for most of the species. For the linear $^1\Sigma^+$ ground state harmonic frequencies, infrared intensities and isotopic shifts were determined up to the CCSD(T)/TZ2P level of theory to assist in its detection. Nonetheless, the ground state of B_3N has eluded spectroscopic characterization.

Preliminary results from the first spectroscopic study on the B_3N^-/B_3N system were recently reported.[19] In that study, we presented vibrationally resolved anion photoelectron spectra of B_3N^- at 266 nm and assigned the observed features to two transitions between states of B_3N with a linear B–N–B–B arrangement. Due to the lack of information on the electronic structure of B_3N^-, we were, however, unable to assign the observed transitions to specific electronic states. Here, we present the 355 and 266 nm photoelectron spectra of B_3N^-. Aided by electronic structure calculations using density functional and coupled cluster theory, we can give a considerably more detailed assignment of these spectra and confirm that the photoelectron spectrum is dominated by linear–linear transitions. Our results reveal that B_3N^- and B_3N both have complex electronic structure, exhibiting low-lying, higher multiplicity electronic states and nearly isoenergetic candidates for ground state structures of B_3N^- and B_3N. This study represents the continuation of our efforts to systematically study the electronic structure of small boron nitride clusters.[19,20,28]

II. EXPERIMENT

The negative ion tandem time-of-flight (TOF) photoelectron spectrometer used in this study has been described

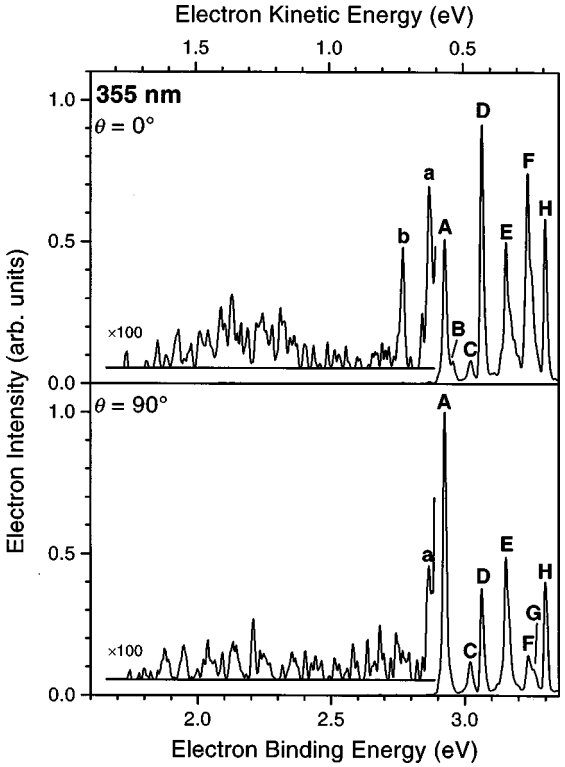

FIG. 1. 355 nm anion photoelectron spectra at $\theta=0°$ (top spectrum) and $\theta=90°$ (bottom spectrum) of B_3N^- plotted against electron binding energy (bottom axis) and electron kinetic energy (top axis). A selected part of the spectra is also shown with a vertical magnification of ×100. Peaks are labeled with letters. Peak positions, asymmetry parameters, and peak assignments are listed in Table I.

previously.[29,30] Boron nitride clusters are prepared by laser ablation with the second harmonic (532 nm, ~30 mJ/pulse) of a Nd:YAG laser tightly focussed onto a rotating and translating ''hot-pressed'' boron nitride disc (Carborundum Corp.). These high laser powers are required to produce boron-rich clusters; at lower powers (~15 mJ/pulse energies), $B_{x+1}N_x^-$ clusters are strongly favored.[19]

The resulting plasma is entrained in a pulse of Ar carrier gas and expanded through a clustering channel. Ions formed in the expansion are extracted perpendicularly to the expansion by means of a pulsed electric field and accelerated to a beam energy of 1.26 keV. The extracted ions enter a linear reflectron time-of-flight mass spectrometer, where they separate in time and space according to their mass-to-charge ratios. The mass resolution is $m/\Delta m \approx 2000$. At the spatial focus of the mass spectrometer, photoelectrons are detached from the mass-selected ions by a fixed frequency laser pulse from a second Nd:YAG laser. The laser firing delay is varied until optimal temporal overlap is achieved with ions of desired mass. The third (355 nm, 3.493 eV, ~140 mJ/cm^2) and fourth harmonics (266 nm, 4.657 eV, ~70 mJ/cm^2) of the second laser were used in this study. The instrument is operated at a repetition rate of 20 Hz. The photoelectron kinetic energy (eKE) is determined by field-free time-of-flight in a 1 m flight tube. All photoelectron spectra presented here are plotted as a function of the electron binding energy (eBE) defined as

$$\mathrm{eBE}=h\nu-\mathrm{eKE}=EA+E_{\mathrm{int}}^{(0)}-E_{\mathrm{int}}^{(-)}, \tag{1}$$

where $h\nu$ denotes the photon energy of the detachment laser, EA the electron affinity of the neutral, and $E_{\mathrm{int}}^{(0)}$ and $E_{\mathrm{int}}^{(-)}$ the internal energies of the neutral and the anion, respectively. At 266 nm, a small amount of background signal from photoelectrons is generated from metal surfaces inside the instrument; this is subtracted from the spectra reported here. This procedure is unnecessary at 355 nm.

This apparatus also yields the angular distribution of the detached photoelectrons, given by

$$\frac{d\sigma}{d\Omega}=\frac{\sigma_{\mathrm{tot}}(\mathrm{eKE})}{4\pi}\left[1+\frac{\beta(\mathrm{eKE})}{2}(3\cos^2\theta-1)\right], \tag{2}$$

where σ_{tot}(eKE) is the total photodetachment cross-section, β(eKE) is the asymmetry parameter ($-1\leqslant\beta\leqslant 2$), and θ measures the angle between the direction of the ejected electron and the polarization of the incident light.[31] θ is varied by means of a 1/4-wave plate. For each feature in the spectrum, β is determined from

$$\beta=\frac{I_{0°}-I_{90°}}{\frac{1}{2}I_{0°}+I_{90°}}, \tag{3}$$

where $I_{0°}$ and $I_{90°}$ are the photoelectron intensities at $\theta=0°$ and $\theta=90°$.[32] In the absence of vibronic coupling and resonances in the photodetachment cross-section, β is not

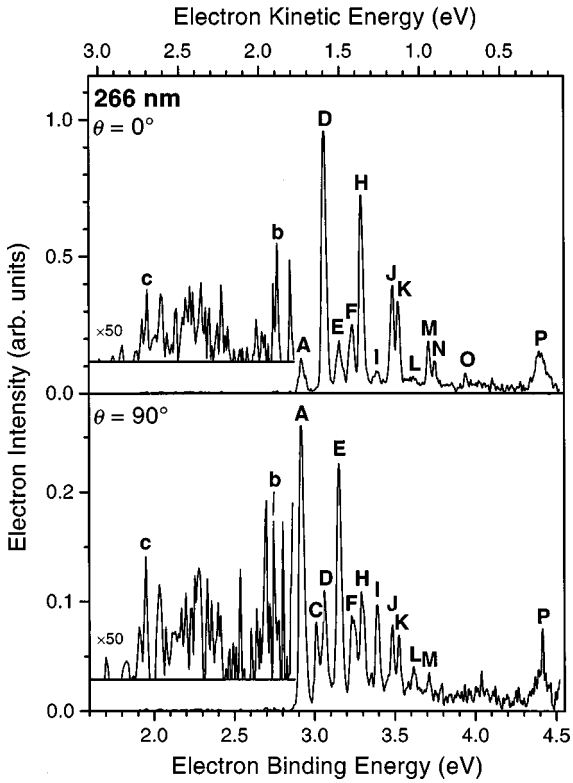

FIG. 2. 266 nm anion photoelectron spectra at $\theta=0°$ (top spectrum) and $\theta=90°$ (bottom spectrum) of B_3N^- plotted against electron binding energy (bottom axis) and electron kinetic energy (top axis). A selected region of both spectra is shown at a magnification of ×50. Peaks are labeled with letters. Peak positions, asymmetry parameters, and peak assignments are listed in Table I.

TABLE I. Electron binding energies (in eV) of peak maxima, asymmetry parameters β and peak assignments for the 355 and 266 nm photoelectron spectra of B_3N^-. Averaged experimental peak positions (Exp.) are also listed.

Peak	355 nm $\theta=0°$	355 nm $\theta=90°$	β_{355}	266 nm $\theta=0°$	266 nm $\theta=90°$	β_{266}	Exp.	Assignment
c	1.929	1.948	+0.1	1.961	1.951	+0.6	1.947	$0_0^0(^2\Pi\rightarrow{}^1\Sigma^+)$
b	2.769	2.768	+1.0	2.772	2.778	+1.4	2.772	$0_0^0(^2\Pi\rightarrow{}^3\Pi)$
a	2.867	2.867	+0.3				2.867	$3_0^1(^2\Pi\rightarrow{}^3\Pi)$
A	2.926	2.926	−0.4	2.920	2.920	−0.4	2.923	$0_0^0(^4\Sigma^-\rightarrow{}^3\Pi)$
B	2.956		+0.6	2.948		−0.1	2.952	
C	3.023	3.021	−0.2		3.011	−0.7	3.018	$3_0^1(^4\Sigma^-\rightarrow{}^3\Pi)$
D	3.064	3.063	+0.6	3.062	3.062	+1.5	3.063	$0_0^0(^4\Sigma^-\rightarrow{}^5\Sigma^-)$
E	3.154	3.153	0.0	3.156	3.152	−0.1	3.154	$1_0^1(^4\Sigma^-\rightarrow{}^3\Pi)$
F	3.234	3.236	+1.2	3.239	3.239	+0.8	3.237	$2_0^1(^4\Sigma^-\rightarrow{}^5\Sigma^-)$
G		3.255	+0.8				3.255	$1_0^13_0^1(^4\Sigma^-\rightarrow{}^3\Pi)$
H	3.299	3.299	+0.3	3.295	3.291	+1.3	3.296	$1_0^1(^4\Sigma^-\rightarrow{}^5\Sigma^-)$
I				3.396	3.392	−0.2	3.394	$1_0^2(^4\Sigma^-\rightarrow{}^3\Pi)$
J				3.489	3.486	+1.2	3.488	$1_0^12_0^1(^4\Sigma^-\rightarrow{}^5\Sigma^-)$
K				3.523	3.526	+1.1	3.525	$1_0^2(^4\Sigma^-\rightarrow{}^5\Sigma^-)$
L				3.617	3.617	+0.3	3.617	$1_0^3(^4\Sigma^-\rightarrow{}^3\Pi)$
M				3.714	3.714	+1.2	3.714	$1_0^22_0^1(^4\Sigma^-\rightarrow{}^5\Sigma^-)$
N				3.750	3.750	+1.3	3.750	$1_0^3(^4\Sigma^-\rightarrow{}^5\Sigma^-)$
O				3.942		+1.3	3.942	$1_0^32_0^1(^4\Sigma^-\rightarrow{}^5\Sigma^-)$
P				4.40	4.42	+0.5	4.41	

expected to change rapidly for transitions to a single electronic state but can vary for transitions to different electronic states.

III. RESULTS

A. Photoelectron spectra

The 355 and 266 nm photoelectron spectra of B_3N^- at $\theta=0°$ (top spectrum) and $\theta=90°$ (bottom spectrum) are shown in Fig. 1 and 2. The photoelectron signal is plotted as a function of eBE (bottom axis) and eKE (top axis). The major peaks occur at eBE$\geqslant$2.9 eV and are labeled with capital letters (A–P). Very weak signal, roughly a factor of 50–100 less intense than the prominent features in Figs. 1 and 2, is observed between 1.7 and 2.9 eV. Selected peaks in this region of the spectrum are labeled with small letters (a–c). Peak positions, asymmetry parameters, and peak assignments are listed in Table I.

The first major peak, peak A, characterized by a negative asymmetry parameter of $\beta_{355\text{nm}}=\beta_{266\text{nm}}=-0.4$, is the most intense peak in the $\theta=90°$ spectra. It is assigned to the origin of an electronic transition yielding an adiabatic detachment energy (ADE) of 2.923 ± 0.008 eV. The ADE is defined as the energy difference between the $v=0$ levels of the anion and neutral electronic states, and is equal to the electron affinity only if both are ground states which, as shown below, is *not* the case here. Peaks B–O are characterized by at least two sets of asymmetry parameters, indicating the presence of a second electronic transition with a considerably different angular distribution. Peak D is the first strong feature after A with a very different anisotropy parameter ($\beta_{355\text{nm}}=+0.6$, $\beta_{266\text{nm}}=+1.5$), so it is assigned as the origin of the second electronic transition, giving an ADE of 3.063 ± 0.008 eV. The difference in the asymmetry parameters for peak D at 355 and 266 nm indicates a rather strong dependence of β for this transition on the eKE.

Most of the remaining strong peaks are attributed to vibrational progressions associated with the two electronic transitions. The extent of these progressions indicates considerable change in the equilibrium geometries upon photodetachment for both transitions. Although the progressions overlap, peaks can generally be identified with a particular electronic transition based on their β-value, since vibrational progressions are usually characterized by an asymmetry parameter similar to that of the band origin.

More detailed vibrational assignments can be made on the basis of the observed peak spacings and intensities. Excitation of two vibrational modes is observed for the first electronic transition, which is characterized by near zero or negative asymmetry parameters. Peaks E, I, and L are assigned to the first three members of a pronounced vibrational progression with a fundamental frequency of $1863\pm60\,\text{cm}^{-1}$. Peak C is assigned to the $v=1$ level of a second mode, yielding a frequency of $758\pm60\,\text{cm}^{-1}$. Excitation in two modes is also observed for the second electronic transition, characterized by large, positive asymmetry parameters. Peaks H, K, and N are assigned to excitation of the first three levels of a mode with a frequency of $1879\pm60\,\text{cm}^{-1}$, while peak F is assigned to excitation of a single quantum in a second vibrational mode ($1403\pm60\,\text{cm}^{-1}$). Peaks J, M, and O may then be attributed to combination bands involving these two modes. However, these peaks are slightly higher in energy and more intense than one would derive from the peaks assigned to the fundamentals and overtones. The broad, unstructured band labeled P lies well above peaks A–O and is attributed to a third electronic transition.

Extremely weak signal compared to peaks A to P is observed at eBE$\leqslant$2.9 eV. The signal onset in the 355 nm spec-

tra, which are background-free with respect to electrons detached from the instrument surface, lies at 1.74 eV. The background-subtracted 266 nm spectra also reveal an onset in signal around 1.7 to 2.0 eV, with peak c being the first large peak in this energy range. The two 355 nm spectra show two sharp features, labeled a and b, slightly below peak A. Peak b is also observed in the 266 nm spectra, while peak a is engulfed by the large signal from peak A. The structure observed between 1.7 and 2.9 eV is similar, but not identical in the 266 and 355 nm spectra. This weak signal is attributed to hot bands, i.e., transitions from excited levels of the anion. The extent and structure of the signal clearly suggests electronic (in addition to vibrational) hot bands, indicating that even more electronic transitions contribute to the spectra.

B. Electronic structure calculations

The experimental photoelectron spectra are quite complex, consisting of overlapped bands that involve multiple anion and neutral electronic states. We have therefore carried out electronic structure calculations to aid in identifying the electronic states and assigning the observed vibrational structure.

Electronic structure calculations were carried out with the GAUSSIAN program packages.[33,34] Calculations with GAUSSIAN92 were performed on a Silicon Graphics Octane workstation at the University of California in Berkeley. GAUSSIAN94 calculations were performed on the Cray J90 SE cluster at the National Energy Research Scientific Computing Center (NERSC) at the Lawrence Berkeley National Laboratory.

The correlation consistent polarized valence basis sets of Dunning and co-workers,[35] denoted by cc-pVxZ, where x = D (double zeta) and T (triple zeta) were used. Additional diffuse functions are especially important for the description of the electronic structure of molecular anions and we therefore predominantly used the augmented correlation consistent sets of Kendall *et al.*,[36] denoted by aug-cc-pVxZ (x = D,T). Geometries and harmonic frequencies were determined using density functional theory (DFT) and coupled cluster theory. The DFT calculations were performed using the B3LYP (Becke-3-parameter-Lee–Yang–Parr) exchange-correlation functional.[37,38] For the coupled cluster calculations we used the CCSD(T) method,[39] where CCSD(T) stands for the coupled cluster with all single and double substitutions (CCSD)[40] augmented with a perturbative estimate of connected triple excitations. For all states presented here, the T_1 diagnostic, which is a rough measure of the importance of nondynamical correlation effects, was performed.[41] A sufficiently small T_1 value ($< \sim 0.02$) indicates that the CCSD(T) relative energies should be close to the full CI energies.

In order to characterize the low-lying electronic states, we first scanned the configurational space at the computationally less demanding B3LYP/aug-cc-pVDZ level of theory. For each stationary point located, harmonic frequencies were determined analytically. In cases where the vibrational analysis yielded imaginary frequencies, the imposed symmetry constraints were relaxed and the calculation repeated at lower symmetry. For selected solutions, geometries and frequencies were also determined employing the more flexible aug-cc-pVTZ basis set. The B3LYP model often yields geometries and frequencies that are in good agreement with experiment. While calculated adiabatic electron affinities (EAs) are generally within ± 0.26 eV of the experimental value, the deviation can be larger than 1 eV.[42,43] In order to get a more reliable estimate of the energetics of the B_3N^-/B_3N system, particularly the adiabatic detachment energies (ADEs), we also determined minimum geometries and harmonic frequencies of selected states at the CCSD(T) level of theory. Harmonic frequencies were determined by double numerical differentiation. It has been shown that CCSD(T)/aug-cc-pVTZ yields electron affinities for the Gaussian-2 collection of atoms and molecules with an absolute error of $\leqslant \pm 0.15$ eV.[44]

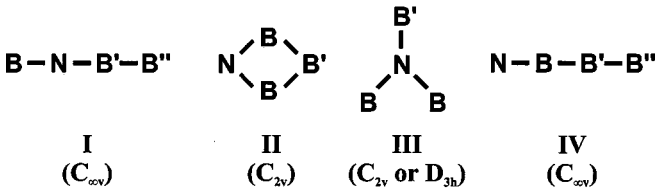

FIG. 3. Four structural isomers with stationary points on the lowest potential energy surfaces of B_3N and B_3N^-. Lines between atoms are shown to aid the eye and do not necessarily reflect the bond properties.

1. Anion manifold

The structure of the B_3N^- anion is unknown. Similar to the previous theoretical study on neutral B_3N by Slanina *et al.*[26] we included various one-, two-, and three-dimensional arrangements of B_3N^- in the survey study. Geometry optimizations involving three-dimensional structures all converged to planar species. We finally arrived at four structural candidates shown in Fig. 3. The B3LYP and CCSD(T) optimized geometries and harmonic frequencies of selected minimum-energy structures are listed in Table II.

The lowest energy isomer is the linear B–N–B–B species (labeled I in Fig. 3, $C_{\infty v}$ spatial symmetry). B_3N^- is predicted by both models to have a quartet ($^4\Sigma^-$) ground state with $\cdots(1\pi)^4(8\sigma)^2(9\sigma)^1(2\pi)^2$ electron occupancy; these four molecular orbitals are shown in Fig. 4. The $^4\Sigma^-$ state is calculated to lie 0.15 eV (including the zero-point vibrational energy correction) below the lower multiplicity $^2\Pi$ state at the CCSD(T)/aug-cc-pVTZ level of theory. The B–N bond lengths in both states are similar, while the B–B bond is more than 0.1 Å longer in the $^2\Pi$ state. The seven normal vibrations of linear B–N–B–B consist of three totally symmetric stretching modes ($\nu_1-\nu_3$) and two doubly degenerate bending modes ($\nu_4-\nu_5$). The calculated harmonic frequencies for the ν_1 and ν_5 modes of the $^4\Sigma^-$ and the $^2\Pi$ states are similar, while those for the other modes are 120–150 cm^{-1} lower in the $^2\Pi$ state.

The next lowest isomer of B_3N^- is the rhombic species II (C_{2v} symmetry). Again, a quartet state ($^4B_1$) is calculated

TABLE II. Calculated electronic term energies ΔE_e and ΔE_0 (in eV), bond lengths r (in Å), bond angles α (in deg), harmonic frequencies (in cm^{-1}), spin ($\langle S^2 \rangle$) for optimized structures of B_3N^- employing aug-cc-pVDZ (AD) and aug-cc-pVTZ (AT) basis sets. For CCSD(T) calculations the value of the T_1 diagnostic is shown.

Species[a]		Method	ΔE_e[b]	ΔE_0	r_{BN}	$r_{NB'}$	$r_{B'B''}$		Harmonic frequencies			$\langle S^2 \rangle$	$\langle T_1 \rangle$
I ($C_{\infty v}$)	$^4\Sigma^-$	B3LYP/AT	0.000	0.000	1.319	1.324	1.544		1832, 1382, 796(σ)	436, 157 (π)		3.75	···
		CCSD(T)/AT[c]	0.000	0.000	1.332	1.332	1.560		1772, 1330, 765 (σ)	422, 123 (π)		3.76	0.025
	$^2\Pi$	B3LYP/AT	0.153	0.115	1.331	1.310	1.672		1837, 1267, 656 (σ)	276, 136 (π)		0.75	···
		CCSD(T)/AT[c]	0.188	0.151	1.343	1.320	1.690		1770, 1211, 625 (σ)	258, 117 (π)		0.76	0.021
					r_{NB}	$r_{BB'}$	r_{BB}	α_{BNB}					
II (C_{2v})	$^4B_1$	B3LYP/AT	0.593	0.589	1.404	1.643	1.671	73.0	1320, 1018, 852 (a_1)	855, 582 (b_2)	499 (b_1)	3.77	···
		CCSD(T)/AT[c]	0.505	0.502	1.419	1.664	1.688	72.0	1251, 984, 817 (a_1)	807, 562(b_2)	479 (b_1)	3.85	0.033
	$^2B_2$	B3LYP/AD	0.845	0.759	1.411	1.761	2.649[d]	139.8	1048, 522, 441 (a_1)	968, 518 (b_2)	297 (b_1)	0.77	···
					$r_{NB'}$	r_{NB}		$\alpha_{BNB'}$					
III (C_{2v})	$^4A_2$	B3LYP/AD	1.839	1.780	1.362	1.506		148.6	1351, 1137, 737 (a_1)	574, 138 (b_2)	307 (b_1)	3.76	···
					r_{NB}	$r_{BB'}$	$r_{B'B''}$						
IV ($C_{\infty v}$)	$^4\Sigma^-$	B3LYP/AD	0.993	0.978	1.286	1.588	1.543		1787, 1334, 648 (σ)	422, 176 (π)		3.79	···
	$^2\Pi$	B3LYP/AD	1.531	1.472	1.285	1.582	1.668		1822, 1172, 591 (σ)	248, 76 (π)		0.76	···

[a]See Fig. 1.
[b]E_{tot}(B3LYP/AD)=−129.209 088 a.u. E_{tot}(B3LYP/AT)=−129.237 038 a.u. E_{tot}(CCSD(T)/AT)=−128.917 719 a.u.
[c]CCSD(T) harmonic frequencies were calculated at the CCSD(T)/AD level of theory.
[d]$r_{NB'}$=1.645 Å.

below the lowest doublet state ($^2B_2$). The geometries and bond properties of these two species are very different. In the $^4B_1$ state, the symmetry-equivalent B atoms are separated by only 1.67 Å and the structure resembles an equilateral BBB triangle with an N atom attached to one of the sides of the triangle. In contrast, the $^2B_2$ state is characterized by larger distance between the equivalent B atoms (r_{BB}=2.65 Å), but the distance between the N atom and the symmetry-unique B atom (r_{NB}) is only 1.65 Å. Energetically higher-lying isomers include a planar isomer with the B atoms arranged triangularly around the center N atom (species III) and the linear N–B–B–B arrangement (species IV). Converged structures involving a BBB triangle with an N atom attached to one of the corners of the triangle were calculated to lie more than 1.75 eV above the $^4\Sigma^-$ state.

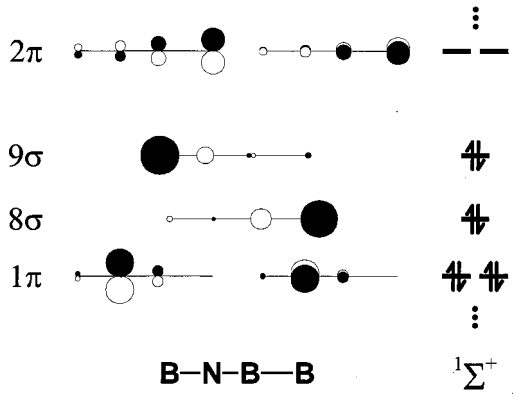

FIG. 4. Highest occupied and lowest unoccupied molecular orbitals (MOs) of the linear B–N–B–B isomer of B_3N plotted using MOPLOT (Ref. 45). The MOs were determined at HF/6-31G level of theory for the $^1\Sigma^+$ state, for which the MO occupancy is shown.

2. Neutral manifold

Previous electronic structure calculations by Slanina *et al.*[25,26] on neutral B_3N predict a $^1\Sigma^+$ ground state with a linear B–N–B–B arrangement. These authors also found an energetically low-lying triangular D_{3h} structure ($^1A_1'$) that, at the G1 level of theory, was only 0.53 eV above the $^1\Sigma^+$ state. A $^3\Sigma^+$ excited state of linear B–N–B–B was calculated 3.2 eV above the $^1\Sigma^+$ state at the QCISD/6-31G* level of theory. Other B_3N arrangements were studied, including linear N–B–B–B and a C_{2v} structure composed of a BBB triangle with the N atom attached from the outside to one of the corners of the triangle.

Our results on the B3LYP and CCSD(T) optimized geometries and harmonic frequencies for selected minimum-energy structures are listed in Table III. The two theoretical models yield contradictory predictions for the lowest energy isomer of B_3N. B3LYP predicts a $^3A_1$ ground state with a rhombic C_{2v} structure (II in Fig. 3). CCSD(T), which predicts relative energies with similar accuracy as G1 theory, finds the closed-shell $^1\Sigma^+$ state to be the lowest-lying electronic state, with the $^3A_1$ state lying 0.09 eV higher in energy (including zero-point energy). Due to the small separation between these two states the ground state of neutral B_3N cannot be unambiguously predicted by either of the two models. This $^3A_1$ state was not considered in the previous theoretical studies.

The $^1\Sigma^+$ state is characterized by a $\cdots(1\pi)^4(8\sigma)^2(9\sigma)^2$ valence orbital occupancy. Several low-lying excited states of linear B–N–B–B have also been characterized for the first time. The lowest excited state is predicted to be a $^3\Pi$ state $[\cdots(1\pi)^4(8\sigma)^2(9\sigma)^1(2\pi)^1]$, lying 0.3–0.6 eV above the $^1\Sigma^+$ state. A $^5\Sigma^-$ state $[\cdots(1\pi)^4(8\sigma)^1(9\sigma)^1(2\pi)^2]$ is found only slightly higher

TABLE III. Calculated electronic term energies ΔE_e and ΔE_0 (in eV), bond lengths r (in Å), bond angles α (in deg), harmonic frequencies (in cm^{-1}), spin ($\langle S^2 \rangle$) for optimized structures of B_3N employing aug-cc-pVDZ (AD), cc-pVTZ (VT), and aug-cc-pVTZ (AT) basis sets. For CCSD(T) calculations the value of the T_1 diagnostic is shown.

Species[a]		Method	ΔE_e[b]	ΔE_0	r_{BN}	$r_{NB'}$	$r_{B'B''}$		ω		$\langle S^2 \rangle$	T_1
I ($C_{\infty v}$)	$^1\Sigma^+$	B3LYP/AT	0.000	0.000	1.378	1.265	1.781		1978, 1136, 580 (σ)	203, 84 (π)	0.00	⋯
		CCSD(T)/VT	0.000	0.000	1.394	1.275	1.789		1949, 1114, 585 (σ)	237, 88 (π)	0.00	0.019
	$^3\Pi$	B3LYP/AT	0.253	0.289	1.368	1.275	1.602		1925, 1212, 750 (σ)	377, 102 (π)	2.00	⋯
		CCSD(T)/VT	0.568		1.387	1.281	1.619		[c]		2.01	0.024
	$^5\Sigma^-$	B3LYP/AT	0.264	0.339	1.264	1.350	1.520		1892, 1506, 810 (σ)	431, 196 (π)	6.02	⋯
		CCSD(T)/VT[d]	0.703	0.764	1.270	1.366	1.530		1887, 1471, 784 (σ)	403, 172 (π)	6.09	0.027
					r_{NB}	$r_{BB'}$	r_{BB}	α_{BNB}				
II (C_{2v})	$^3A_1$	B3LYP/AT	−0.295	−0.235	1.381	1.661	1.731	77.6	1408, 1007, 786 (a_1)	1090, 624 (b_2) 326 (b_1)	2.02	⋯
		CCSD(T)/VT[d]	0.034	0.085	1.396	1.678	1.744	77.3	1367, 982, 779 (a_1)	1041, 601 (b_2) 320 (b_1)	2.16	0.038
	$^1A_1$	B3LYP/AT	0.316	0.326	1.339	1.890	1.910	91.0	1426, 633, 349 (a_1)	1373, 359 (b_2) 280 (b_1)	0.00	⋯
					$r_{NB'}$	r_{NB}		$\alpha_{BNB'}$				
III (C_{2v})	$^3B_2$	B3LYP/AD	0.780	0.783	1.423	1.444		145.6	1393, 1038, 760 (a_1)	863, 80 (b_2) 181 (b_1)	2.01	⋯
					r_{NB}							
III (D_{3h})	$^1A_{1'}$	B3LYP/AD	0.797	0.775	1.453				871 (a_1') 300 (a_2'')	1063, 309 (e')	0.00	⋯
					r_{NB}	$r_{BB'}$	$r_{B'B''}$					
IV ($C_{\infty v}$)	$^3\Pi$	B3LYP/AD	1.932	1.961	1.293	1.545	1.587		1861, 1267, 664 (σ)	354, 122 (π)	2.04	⋯
	$^5\Pi$	B3LYP/AD	2.066	2.096	1.327	1.618	1.538		1660, 1349, 627 (σ)	398, 163 (π)	6.02	⋯
	$^1\Sigma^+$	B3LYP/AD	2.288	2.265	1.284	1.546	1.799		1928, 1089, 530 (σ)	119, 55 (π)	0.00	⋯

[a]See Fig. 1.
[b]E_{tot}(B3LYP/AD)=−129.111 431 a.u. E_{tot}(B3LYP/AT)=−129.137 714 a.u. E_{tot}(CCSD(T)/VT)=−128.826 016 a.u.
[c]No convergence.
[d]CCSD(T) harmonic frequencies were calculated at the CCSD(T)/VD level of theory.

in energy. The bond distances and harmonic bending frequencies are considerably different for these three states of linear B–N–B–B. This is a result of the different number of electrons occupying the 2π orbitals, which are characterized by a bonding interaction for the terminal bonds and an antibonding interacting for the center bond (see Fig. 4). Thus, $r_{B'B''}$ decreases and the ν_4 frequency increases with the number of electrons occupying the 2π orbitals.

In the rhombic geometry, a $^1A_1$ state is found to lie above the $^3A_1$ state. Triangular arrangements of B_3N with a central N atom (species III in Fig. 3) are calculated 0.78 eV above the $^1\Sigma^+$ state. We find two close-lying states for this isomer, a closed shell D_{3h} structure ($^1A_1'$), and an open shell C_{2v} structure ($^3B_2$). Various states of the linear N–B–B–B isomer are found considerably higher in energy. The present results for the B_3N/B_3N^- system are similar to those for the carbon clusters C_4 and C_4^-. While C_4^- is clearly linear, cyclic and linear structures are predicted to lie close in energy for the neutral species.[21]

3. Adiabatic detachment energies

ADEs for the various photodetachment transitions calculated at the B3LYP and CCSD(T) levels of theory are shown in Table IV. The MO from which the electron is detached is also listed. Both theoretical models predict the same ordering of the four calculated linear–linear B–N–B–B transitions. From the $^4\Sigma^-$ anion ground state, only the electronically excited states $^3\Pi$ and $^5\Sigma^-$ of linear B–N–B–B can be accessed via one-electron photodetachment. Both models give similar results for these transitions, i.e., they predict them to be around ~2.9 and ~3.0 eV, respectively. One-electron detachment from the $^2\Pi$ excited state, on the other hand, cannot access the $^5\Sigma^-$ state, but only the $^1\Sigma^+$ and $^3\Pi$ states of linear B–N–B–B. The models disagree on the location of the $^2\Pi \rightarrow {}^1\Sigma^+ + e^-$ transition CCSD(T) predicts $ADE_0 = 2.14$ eV, while the B3LYP model calculates this transition 0.39 eV higher in energy. Both models agree on the $^2\Pi \rightarrow {}^3\Pi + e^-$ transition, which is calculated to lie around 2.75 eV. We also calculated the lowest cyclic-to-cyclic and linear-to-cyclic transitions. The $^4B_1 \rightarrow {}^3A_1 + e^-$ transition is predicted to occur around 1.82 eV, well below the linear-to-linear transitions discussed above. The $^4\Sigma^- \rightarrow {}^3A_1 + e^-$ transition is calculated in the vicinity of the $^2\Pi \rightarrow {}^1\Sigma^+ + e^-$ transition.

IV. ANALYSIS AND DISCUSSION

The major bands in the photoelectron spectra can now be assigned by comparison with the ADEs and vibrational frequencies of the electronic structure calculations. The two electronic transitions with origins at 2.923 eV (peak A) and 3.063 eV (peak D) lie very close to the calculated ADEs at the CCSD(T) level of theory of 2.90 and 3.04 eV for the B–N–B–B linear-to-linear $^4\Sigma^- \rightarrow {}^3\Pi + e^-$ and $^4\Sigma^- \rightarrow {}^5\Sigma^- + e^-$ transitions, respectively. Moreover, the observed fundamental frequencies of the lower energy band, 1863 and 758 cm^{-1}, are close to the calculated ν_1 and ν_3 harmonic frequencies of 1925 and 750 cm^{-1}, respectively, for the $^3\Pi$ state. In the higher energy band, the observed frequencies of

TABLE IV. Calculated adiabatic detachment energies ADE_e and ADE_0 (in eV) for selected transitions of the B_3N^-/B_3N system. The symmetry of the molecular orbital (MO) from which the electron is detached is also listed.

			B3LYP[a]		CCSD(T)[b]	
Species	Transition	MO	ADE_e	ADE_0[c]	ADE_e	ADE_0[c]
I→I	$^2\Pi \rightarrow {}^1\Sigma^+ + e^-$	π	2.550	2.530	2.145	2.141
	$^2\Pi \rightarrow 3\Pi + e-$	σ	2.803	2.819	2.710	
	$^4\Sigma^- \rightarrow {}^3\Pi + e^-$	π	2.956	2.934	2.898	
	$^4\Sigma^- \rightarrow {}^5\Sigma^- + e^-$	σ	2.967	2.984	3.041	3.062
II→II	$^4B_1 \rightarrow {}^3A_1 + e^-$	b_1	1.815	1.822		
I→II	$^4\Sigma^- \rightarrow {}^3A_1 + e^-$	π	2.408	2.411		
III→III	$^4A_2 \rightarrow {}^3B_2 + e^-$	b_1	1.598[d]	1.602[d]		
IV→IV	$^4\Sigma^- \rightarrow {}^3\Pi + e^-$	π	3.597[d]	3.583[d]		

[a]Energies and harmonic frequencies determined at the B3LYP/aug-cc-pVTZ level (see Tables II and III).
[b]Energies determined at the CCSD(T)/aug-cc-pVTZ level of theory. Harmonic frequencies are taken from Tables II and III.
[c]Adiabatic detachment energy including zero-point correction.
[d]Energies and harmonic frequencies determined at the B3LYP/aug-cc-pVDZ level.

1879 and 1403 cm^{-1} match the calculated values of 1887 cm^{-1}(ν_1) and 1471 cm^{-1} (ν_2) for the $^5\Sigma^-$ state. The high ν_1 frequency is characteristic of a linear B_3N species, either B–N–B–B or N–B–B–B, while all two-dimensional structures are predicted to have no vibrational frequencies above 1450 cm^{-1}. We therefore assign the two bands to the aforementioned B–N–B–B transitions. Assignment of these bands to transitions between N–B–B–B structures is far less satisfactory: the $^4\Sigma^-$ N–B–B–B structure for B_3N^- is calculated to lie 0.98 eV above the $^4\Sigma^-$ B–N–B–B structure, the calculated ADEs for the transitions to the $^3\Pi$ and $^5\Sigma^-$ states are far from the experimental values, and the vibrational frequencies do not match as well.

In order to support our assignments, spectral simulations were performed within the Franck–Condon approximation. Based on the B3LYP/aug-cc-pVTZ force constants for the initial state of the anion and the final state of the neutral, we determined the change in normal coordinates between the equilibrium structures of various states of B_3N^- and B_3N within the parallel mode approximation. Simulated spectra were then generated employing the B3LYP/aug-cc-pVTZ harmonic frequencies and equilibrium normal coordinate changes. Transition origins were taken from experiment and only totally-symmetric modes were included in the simulation. Eigenvalues and eigenfunctions were determined analytically assuming harmonic potentials. The eigenfunctions were used to determine the FC factors by numerical integration. The resultant stick spectra were convoluted with the experimental resolution function. We then optimized selected simulation parameters, including the harmonic frequencies of the neutral species, the change in equilibrium normal coordinates (between the anion and the neutral), and the mean ion vibrational temperature, in order to achieve the best agreement with the four experimental spectra. The B3LYP/aug-cc-pVTZ and the optimized simulation parameters are listed in Table V. The optimized mean ion vibrational temperature was 200 K.

The optimized simulations of the main bands are shown together with the experimental spectra in Fig. 5 and 6. These simulated photoelectron spectra are in reasonable agreement with the experimental spectra. The overall structure of the experimental spectra is well reproduced with relatively minor changes required for the parameters derived from the electronic structure calculations. The largest deviation between the DFT and optimized parameters is found for the ν_2 mode of the $^5\Sigma^-$ state, for which the DFT harmonic frequency ω_2 is too high by 81 cm^{-1} and the change in equilibrium normal coordinate ΔQ_2 is underestimated by a factor of 3.5. For the $^4\Sigma^- \rightarrow {}^5\Sigma^- + e^-$ band, the optimized normal coordinate displacement ΔQ_3 was 10% even though no ob-

TABLE V. Calculated (Calc.) and optimized (Exp.) simulation parameters for the simulated photoelectron spectra of B_3N^-. Calculated harmonic frequencies ω_1 (in cm^{-1}) and equilibrium normal coordinate changes $|\Delta Q_i|$ (in percent relative to Q_i of the anion) were determined at the B3LYP/aug-cc-pVTZ level of theory (see text).

Transition		ω_i^{anion}	$\omega_i^{neutral}(\Delta Q_i)$		
$^4\Sigma^- \rightarrow {}^3\Pi + e^-$	Calc.	1832, 1383, 796	1925 (15%),	1212 (1%)	750(13%)
	Exp.		1875 (17%),	1225 (3%),	775 (13%)
$^4\Sigma^- \rightarrow {}^5\Sigma^+ + e^-$	Calc.	1832, 1383, 796	1892 (13%),	1506 (4%),	810 (8%)
	Exp.		1875 (18%),	1425 (14%),	750 (10%)
$^2\Pi \rightarrow {}^1\Sigma^+ + e^-$	Calc.	1837, 1267, 656	1978 (15%),	1136 (1%),	580 (26%)
	Exp.				
$^2\Pi \rightarrow {}^3\Pi + e^-$	Calc.	1837, 1267, 656	1925 (7%),	1212 (12%),	750 (22%)
	Exp.				775

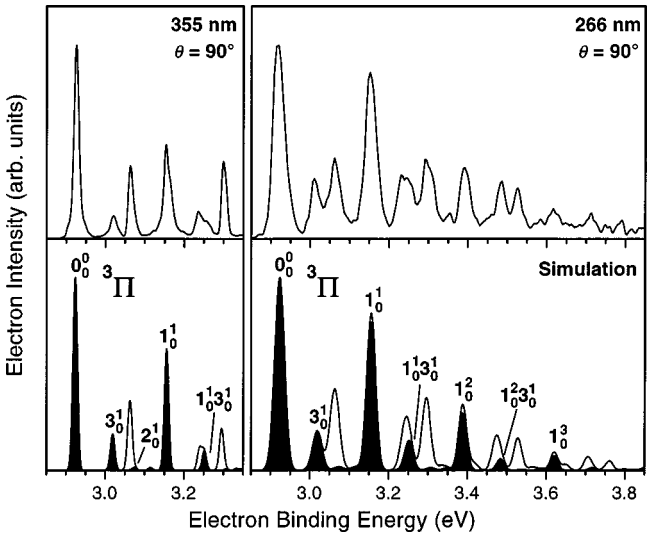

FIG. 5. Experimental (top) and simulated (bottom) 355 and 266 nm photoelectron spectra at $\theta=90°$ of B_3N^- in the eBE region above 2.85 eV. Two electronic transitions, $^4\Sigma^-\rightarrow{}^3\Pi+e^-$ and $^4\Sigma^-\rightarrow{}^5\Sigma^-+e^-$ were included in the simulation (see Table V for optimized simulation parameters). The black shaded area represents the contribution from the $^4\Sigma^-\rightarrow{}^3\Pi+e^-$ transition. Peaks assignments are shown for the $^4\Sigma^-\rightarrow{}^3\Pi+e^-$ transition.

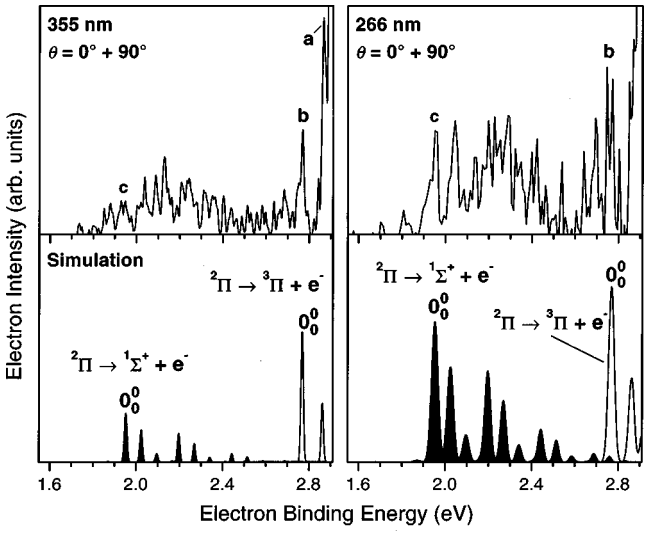

FIG. 7. Experimental (top) and simulated (bottom) 355 and 266 nm photoelectron spectra of B_3N^- in the eBE region below 2.9 eV. Two electronic transitions, $^2\Pi\rightarrow{}^1\Sigma^++e^-$ and $^2\Pi\rightarrow{}^3\Pi+e^-$, were included in the simulation (see Table V for optimized simulation parameters). The black shaded area represents the contribution from the $^2\Pi\rightarrow{}^1\Sigma^++e^-$ transition.

vious progression in the mode appears in the spectrum. The reason for this can be seen in Fig. 6, which shows that the 3_0^1 transition of the $^4\Sigma^-\rightarrow{}^5\Sigma^-+e^-$ band overlaps the 1_0^1 transition of the $^4\Sigma^-\rightarrow{}^3\Pi+e^-$ band. While nearly all peak positions are accurately reproduced, the simulated $1_0^n2_0^1$ combination bands ($n=1,2$) for the $^4\Sigma^-\rightarrow{}^5\Sigma^-+e^-$ band (the major components of peaks J and M) occur at too low an eBE. Several smaller features, including peak B and some of the structure observed to the blue of peak E, do not appear in the simulations. These may involve excitation of the nontotally symmetric lower frequency modes that were excluded from the simulations.

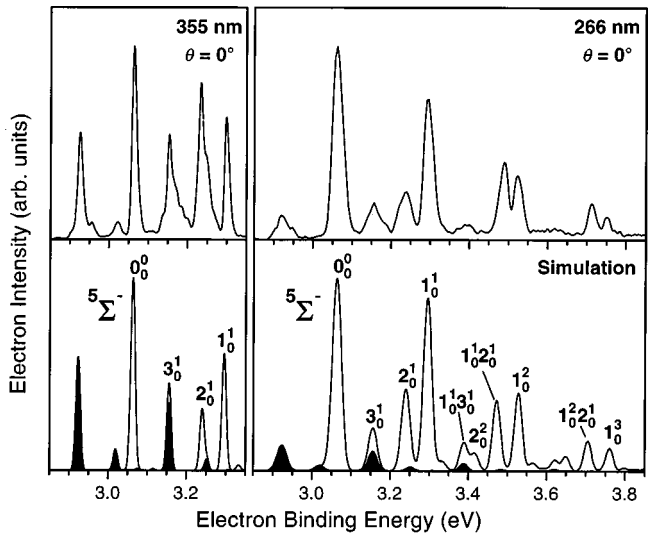

FIG. 6. Experimental (top) and simulated (bottom) 355 and 266 nm photoelectron spectra at $\theta=0°$ of B_3N^- in the eBE region above 2.85 eV. Two electronic transitions, $^4\Sigma^-\rightarrow{}^3\Pi+e^-$ and $^4\Sigma^-\rightarrow{}^5\Sigma^-+e^-$ were included in the simulation (see Table V for optimized simulation parameters). The black shaded area represents the contribution from the $^4\Sigma^-\rightarrow{}^3\Pi+e^-$ transition. Peaks assignments are shown for the $^4\Sigma^-\rightarrow{}^5\Sigma^-+e^-$ transition.

The signal below eBE$=2.9$ eV is very weak but nonetheless real. In Fig. 7 we attempt to simulate this signal assuming it originates from photodetachment of the electronically excited but low-lying $^2\Pi$ state of the anion (B–N–B–B structure). Since $\Delta E_0=0.15$ eV for this state at the CCSD(T) level of theory, it is reasonable to expect nonzero population in our ion beam.

The spectrum in this range was simulated assuming photodetachment of the $^2\Pi$ state. This yields transitions to the neutral $^1\Sigma^+$ ground state and $^3\Pi$ excited state with band origins at 1.947 ± 0.025 eV (peak c) and 2.772 ± 0.010 eV (peak b), respectively. These lie close to the calculated ADEs at the CCSD(T)/aug-cc-pVTZ level of theory for the $^2\Pi\rightarrow{}^1\Sigma^++e^-$ and $^2\Pi\rightarrow{}^3\Pi+e^-$ transitions of 2.14 and 2.71 eV, respectively (Table IV). Calculated frequencies and normal coordinate displacements were used as indicated in Table V.

The agreement between simulation and experiment is clearly much worse than in Figs. 5 and 6, particularly at 355 nm. We attribute much of this to the poor signal-to-noise in the experimental spectra. Nonetheless, there is enough similarity between the experimental and simulated spectra at 266 nm to support the assignment of peak c to the $^2\Pi\rightarrow{}^1\Sigma^++e^-$ origin and peak b to the origin of the $^2\Pi\rightarrow{}^3\Pi+e^-$ transition. Although peaks b and c at first glance appear to be vibrational hot bands of the intense $^4\Sigma^-\rightarrow{}^3\Pi+e^-$ transition, they are assigned as the origin and 3_0^1 transitions of the $^2\Pi\rightarrow{}^3\Pi+e^-$ band for three reasons. (i) The 355 and 266 nm asymmetry parameters of peak b do not reflect the angular behavior of the origin of the $^4\Sigma^-\rightarrow{}^3\Pi+e^-$ transition. Large positive asymmetry parameters *are* expected for the $^2\Pi\rightarrow{}^3\Pi+e-$ transition, as the electron is removed from the same σ orbital as for the $^4\Sigma^-\rightarrow{}^5\Sigma^-+e^-$ transition, which is characterized by large positive asymmetry parameters. (ii)

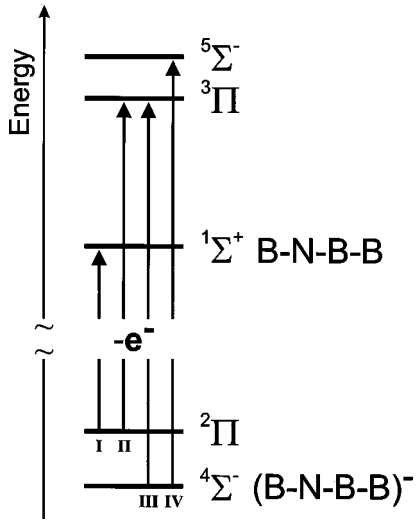

FIG. 8. Schematic of photodetachment transitions (labeled I–IV) observed in the photoelectron spectra of B_3N^-.

The calculated ADE is in excellent agreement with the position of peak b. (iii) The spacing between peaks b and a (766 cm^{-1}) is in excellent agreement with B3LYP/aug-cc-pVTZ harmonic frequency for the ν_3 mode of the $^3\Pi$ state (750 cm^{-1}).

The ADE of the linear-to-cyclic $^4\Sigma^- \rightarrow {}^3A_1 + e^-$ transition at the B3LYP/aug-cc-pVTZ level is 2.41 eV. However, based on poor Franck–Condon overlap this transition is expected to be extremely weak and broad without much structure. We thus believe that the rather sharp structures observed are not due to this transition. On the other hand, the observed signal onset at 1.74 eV in the 355 nm spectra may originate from the cyclic-to-cyclic $^4B_1 \rightarrow {}^3A_1 + e^-$ transition, for which the calculated ADE is 1.82 eV.

We close by determining the EA of B_3N. This is complicated by two factors. First, the identity of the lowest energy structure of neutral B_3N and thus its electronic ground state is uncertain. For purposes of this discussion, we assume that the calculated energy ordering of B_3N structures at the CCSD(T) is correct (Table III) so that the linear B–N–B–B $^1\Sigma^+$ state lies slightly below the cyclic $^3A_1$ state. The EA would then be the vibrational origin of the $^4\Sigma^- \rightarrow {}^1\Sigma^+ + e^-$ photodetachment transition which, unfortunately, is not seen as it is not a one-electron transition. However, we have enough information on the anion and neutral energetics from our assignments of the photoelectron spectra to extract the electron affinity using the scheme in Fig. 8. The electronic term energy T_0 of the $^2\Pi$ state is 0.151 ± 0.010 eV, given by the difference of the ADEs of the $^4\Sigma^- \rightarrow {}^3\Pi + e^-$ and $^2\Pi \rightarrow {}^3\Pi + e^-$ transitions (III−II in Fig. 8). The EA of linear B–N–B–B can then be determined from the ADE of the $^2\Pi \rightarrow {}^1\Sigma^{-+} + e^-$ transition and is 2.098 ± 0.035 eV (III−II+I). With this value the term energies T_0 of the $^3\Pi$ and $^5\Sigma^-$ states are 0.825 and 0.965 eV, respectively. Although this analysis depends on our assignment of the weak features in Fig. 7, the derived values are certainly close to those obtained at the highest level of theory employed in the present study, namely 0.15 eV for the term energy of the $^2\Pi$ state and 2.29 eV for the EA.

ACKNOWLEDGMENTS

This research is supported by the National Science Foundation under Grant No. DMR-9814677. K. R. A. gratefully acknowledges a postdoctoral fellowship from the Swiss National Science Foundation. This research used resources of the National Energy Research Scientific Computing Center, which is supported by the Office of Science of the U.S. Department of Energy under Contract No. DE-AC03-76SF00098. Special appreciation is expressed to Dr. Stephan Matzinger for helpful discussions.

[1] P. B. Mirkarimi, K. F. McCarty, and D. L. Medlin, Mater. Sci. Eng., R. **21**, 47 (1997).
[2] S. H. Yang, C. L. Pettiette, J. Conceicao, O. Cheshnovsky, and R. E. Smalley, Chem. Phys. Lett. **139**, 233 (1987).
[3] S. Yang, K. J. Taylor, M. J. Craycraft, J. Conceicao, C. L. Pettiette, O. Cheshnovsky, and R. E. Smalley, Chem. Phys. Lett. **144**, 431 (1988).
[4] D. W. Arnold, S. E. Bradforth, T. N. Kitsopoulos, and D. M. Neumark, J. Chem. Phys. **95**, 8753 (1991).
[5] H. Kietzmann, R. Rochow, G. Gantefor, W. Eberhardt, K. Vietze, G. Seifert, and P. W. Fowler, Phys. Rev. Lett. **81**, 5378 (1998).
[6] N. G. Gotts, G. Von Helden, and M. T. Bowers, Int. J. Mass Spectrom. Ion Processes **149–150**, 217 (1995).
[7] J. C. Grossman, L. Mitas, and K. Raghavachari, Phys. Rev. Lett. **75**, 3870 (1995).
[8] N. G. Chopra, R. J. Luyken, K. Cherrey, V. H. Crespi, M. L. Cohen, S. G. Louie, and A. Zettl, Science **269**, 966 (1995).
[9] A. Loiseau, F. Willaime, N. Demoncy, G. Hug, and H. Pascard, Phys. Rev. Lett. **76**, 4737 (1996).
[10] K. Suenaga, C. Carbon, N. Demoncy, and A. Loiseau, Science **278**, 653 (1997).
[11] F. Banhart, M. Zwanger, and H.-J. Muhr, Chem. Phys. Lett. **231**, 98 (1994).
[12] L. Boulanger, B. Andriot, M. Cauchetier, and F. Willaime, Chem. Phys. Lett. **234**, 227 (1995).
[13] O. Stephan, Y. Bando, A. Loiseau, F. Willaime, N. Schramchenko, T. Tamiya, and T. Sato, Appl. Phys. A: Mater. Sci. Process. **67**, 107 (1998).
[14] L. Andrews and P. Hassanzadeh, J. Phys. Chem. **96**, 9177 (1992).
[15] L. B. Knight, D. W. Hill, T. J. Kirk, and C. A. Arrington, J. Phys. Chem. **96**, 555 (1992).
[16] L. Andrews, P. Hassanzadeh, T. R. Burkholder, and J. M. L. Martin, J. Chem. Phys. **98**, 922 (1993).
[17] C. A. Thompson, L. Andrews, J. M. L. Martin, and J. El-Yazal, J. Phys. Chem. **99**, 13839 (1995).
[18] C. A. Thompson and L. Andrews, J. Am. Chem. Soc. **117**, 10125 (1995).
[19] K. R. Asmis, T. R. Taylor, and D. M. Neumark, Eur. Phys. J. D (in press).
[20] K. R. Asmis, T. R. Taylor, and D. M. Neumark, J. Chem. Phys. (in press).
[21] K. Raghavachari and J. S. Binkley, J. Chem. Phys. **87**, 2191 (1987).
[22] S. Becker and H.-J. Dietze, Int. J. Mass Spectrom. Ion Processes **73**, 157 (1986).
[23] G. Seifert, B. Schwab, S. Becker, and H.-J. Dietze, Int. J. Mass Spectrom. Ion Processes **85**, 327 (1988).
[24] P. A. Roland and J. J. Wynne, J. Chem. Phys. **99**, 8599 (1993).
[25] Z. Slanina, J. M. L. Martin, J.-P. François, and R. Gijbels, Chem. Phys. **178**, 77 (1993).
[26] Z. Slanina, J. M. L. Martin, J.-P. François, and R. Gijbels, Chem. Phys. Lett. **201**, 54 (1993).
[27] J. M. L. Martin, Z. Slanina, J.-P. François, and R. Gijbels, Mol. Phys. **82**, 155 (1994).
[28] K. R. Asmis, T. R. Taylor, and D. M. Neumark, Chem. Phys. Lett. **295**, 75 (1998).
[29] R. B. Metz, A. Weaver, S. E. Bradforth, T. N. Kitsopoulos, and D. M. Neumark, J. Phys. Chem. **94**, 1377 (1990).
[30] C. Xu, G. R. Burton, T. R. Taylor, and D. M. Neumark, J. Chem. Phys. **107**, 3428 (1997).
[31] J. Cooper and R. N. Zare, J. Chem. Phys. **48**, 942 (1968).

[32] K. M. Ervin and W. C. Lineberger, in *Advances in Gas Phase Ion Chemistry*, edited by N. G. Adams and L. M. Babcock (JAI, Greenwich, CT, 1992), Vol. 1.
[33] GAUSSIAN 92, M. J. Frisch, G. W. Trucks, M. Head-Gordon, P. M. W. Gill, M. W. Wong, J. B. Foresman, B. G. Johnson, H. B. Schlegel, M. A. Robb, E. S. Replogle, R. Gomperts, J. L. Andres, K. Raghavachari, J. S. Binkley, C. Gonzalez, R. L. Martin, D. J. Fox, D. J. Defrees, J. Baker, J. J. P. Stewart, and J. A. Pople, Gaussian, Inc., Pittsburgh, pp. 1992.
[34] GAUSSIAN 94, M. J. Frisch, G. W. Trucks, H. B. Schlegel, P. M. W. Gill, B. G. Johnson, M. A. Robb, J. R. Cheeseman, T. Keith, G. A. Petersson, J. A. Montgomery, K. Raghavachari, M. A. Al-Laham, V. G. Zakrzewski, J. V. Ortiz, J. B. Foresman, J. Cioslowski, B. B. Stefanov, A. Nanayakkara, M. Challacombe, C. Y. Peng, P. Y. Ayala, W. Chen, M. W. Wong, J. L. Andres, E. S. Replogle, R. Gomperts, R. L. Martin, D. J. Fox, J. S. Binkley, D. J. Defrees, J. Baker, J. P. Stewart, M. Head-Gordon, C. Gonzalez, and J. A. Pople, Gaussian, Inc., Pittsburgh, PA, 1995.
[35] T. H. Dunning, Jr., J. Chem. Phys. **90**, 1007 (1989).
[36] R. A. Kendall, T. H. Dunning, Jr., and R. J. Harrison, J. Chem. Phys. **96**, 6796 (1992).
[37] C. Lee, W. Yang, and R. G. Parr, Phys. Rev. B **37**, 785 (1988).
[38] A. D. Becke, J. Chem. Phys. **98**, 5648 (1993).
[39] K. Raghavachari, G. W. Trucks, J. A. Pople, and M. Head-Gordon, Chem. Phys. Lett. **157**, 479 (1989).
[40] G. D. Purvis III and R. J. Bartlett, J. Chem. Phys. **76**, 1910 (1982).
[41] T. J. Lee and P. R. Taylor, Int. J. Quantum Chem., Quantum Chem. Symp. **23**, 199 (1989).
[42] G. S. Tschumper and H. F. Schaefer III, J. Chem. Phys. **107**, 2529 (1997).
[43] L. A. Curtiss, P. C. Redfern, K. Raghavachari, and J. A. Pople, J. Chem. Phys. **109**, 42 (1998).
[44] D. Feller and K. A. Peterson, J. Chem. Phys. **108**, 154 (1998).
[45] A. Schmelzer and E. Haselbach, Helv. Chim Acta **54**, 1299 (1971) (the present improved version of the program has been written by T. Bally).